

Numerical and experimental characterization of a novel modular passive micromixer

Francesco Pennella Massimiliano Rossi
Simone Ripandelli Marco Rasponi
Francesco Mastrangelo Marco A. Deriu
Luca Ridolfi Christian J. Kähler
Umberto Morbiducci

ABSTRACT This paper reports a new low-cost passive microfluidic mixer design, based on a replication of identical mixing units composed of microchannels with variable curvature (clothoid) geometry. The micromixer presents a compact and modular architecture that can be easily fabricated using a simple and reliable fabrication process. The particular clothoid-based geometry enhances the mixing by inducing transversal secondary flows and recirculation effects. The role of the relevant fluid mechanics mechanisms promoting the mixing in this geometry were analysed using computational fluid dynamics (CFD) for Reynolds numbers ranging from 1 to 110. A measure of mixing potency was quantitatively evaluated by calculating mixing efficiency, while a measure of particle dispersion was assessed through the lacunarity index. The results show that the secondary flow arrangement and recirculation effects are able to provide a mixing efficiency equal to 80 % at Reynolds number above 70. In addition, the analysis of particles distribution promotes the lacunarity as powerful tool to quantify the dispersion of fluid particles and, in turn, the overall mixing. On fabricated micromixer prototypes the microscopic- Laser-Induced-Fluorescence (μ LIF) technique was applied to characterize mixing. The experimental results confirmed the mixing potency of the microdevice.

Keywords Microfluidic mixer . Clothoid microchannel .
Microfluidics . Computational fluid dynamics .
Microscopic-Laser-Induced-Fluorescence

1 Introduction

Mixing is a crucial issue in microfluidic systems where the optimization of chemical and biochemical reactions must be obtained. Indeed, in recent years great effort has been put in the development of microfluidic devices, the so-called micromixers, able to effectively induce mixing (Hardt et al. 2005).

In particular, microfluidic mixers have attracted considerable attention for applications in the biomedical field such as Lab-on-a-chip and micro-total-analysis systems (Lin et al. 2007; Chung et al. 2008; Marasso et al. 2011). Two are the main phenomena occurring within microfluidic mixers, i.e., diffusion and convective transport. Under laminar flow (microfluidics is mostly characterized by laminar flow and cannot take advantage of turbulence to improve mixing efficiency) mixing is mainly a diffusive phenomenon, which can be problematic because the time required for mixing increases with the power of the diffusion length and can be prohibitive: when mixing is merely due to diffusive effects, adequate length is needed (Sudarsan and Ugaz 2006), yielding strict constraints on overall dimensions. To amplify the diffusive phenomenon, chaotic advection is widely exploited in microfluidics and can be obtained by varying the velocity along a streamline in three dimensions, thus generating a chaotic process of folding and stretching of the interface between miscible streams that reduces the diffusive length and increases overall mixing efficiency. This process occurs at even very low Reynolds numbers (Stroock et al. 2002). Chaotic advection can be generated in micromixers designed to perturb the laminar flow properly. These microdevices can be classified taking in consideration both (1) flow regimes (Nguyen and Wu 2005; Nguyen 2008) and (2) geometric features (Chung and Shih 2008). As for point (1), three subgroups can be considered, depending on flow regime: (a) at relatively high Reynolds number, (b) at intermediate Reynolds numbers and (c) at low Reynolds numbers (Nguyen and Wu 2005). In the literature, micromixers are classified as either active or passive. Active micromixers use external power sources to enhance mixing, such as external variable-frequency pumping (Niu and Lee 2003) or bubble-induced acoustic microstreaming (Liu et al. 2002). On the contrary passive micromixers, which are the object of this study, exploit geometric features for mixing generation and present the advantage that they can be readily integrated and interfaced with other microfluidic components (Pennella et al. 2011). For passive micromixers, an effective design of the geometry of the microdevice becomes crucial. For this reason, recent research has been focused on enhancing mixing by properly increasing chaotic advection and/or convective transport in ad hoc designed microdevices. Most passive micromixer designs are based on flow lamination (Nguyen and Wu 2005). The principle of flow lamination relies on the ability to increase the interfacial area between the mixing fluids, thus reducing both mixing space and time lengths (Bessoth et al. 1999; Löb et al. 2004). For example, this kind of micromixers apply the principle of multi-lamination, with microchannels that allow several cycles of splitting and recombination of the fluid streams (Kim et al.

2005). Chaotic advection mixing has been often achieved through three-dimensional designs (Liu et al. 2000; Lin et al. 2007), the implementation of topological features to microchannels (Stroock et al. 2002) and the use of planar microchannels (Schönfeld and Hardt 2004; Sudarsan and Ugaz 2006; Gigras and Pushpavanam 2008; Chung et al. 2008; Ansari et al. 2010). As an example, Liu and coworkers (Liu et al. 2000) proposed a three-dimensional serpentine microchannel design characterized by two perpendicular C-shaped mixing segments, to generate chaotic advection. Another approach was proposed by Stroock et al. (2002), with a micromixer design based on the addition of grooves on top of microchannels wall, which create chaotic advection assuring satisfactory mixing potency at low and intermediate Reynolds numbers (Stroock et al. 2002). Also micromixers based on inertial effects can be classified as chaotic advection devices (Nguyen and Wu 2005; Hessel et al. 2005; Nguyen 2008) and belong to the intermediate/relatively high Reynolds number subgroups. This class of micromixers is represented by curved microchannels, where at certain flow regimes the onset of Dean vortices (due to the centrifugal forces) enhances fluid convective mixing (Howell et al. 2004). Several micromixer designs have been proposed that take advantage of the onset of secondary flows: spiral microchannels (Sudarsan and Ugaz 2006), U-shaped microchannels (Gigras and Pushpavanam 2008), rhombic cells micromixers or circular cell (Chung and Shih 2007; Chung et al. 2008; Chung et al. 2010; Ansari et al. 2010) where mixing is improved by the combined effect of focusing/ diverging, obstacles, different sub-channel widths and Dean vortices and contraction-expansion array microchannel employing a combination of expansion-vortices and Dean vortices (Lee et al. 2010). A main limitation to the application of the class of micromixers based on inertial effects is that either relatively high Reynolds numbers (Schönfeld and Hardt 2004; Gigras and Pushpavanam 2008) and/or high channel lengths (Howell et al. 2004), are needed to perform mixing. In this study we propose a novel low-cost planar passive microfluidic mixer design. The micromixer is based on a variable (i.e., clothoid-based) curvature design unit cell, which is easy to fabricate and integrate due to the high modularity of the unit cells. The design of the device is driven also by the flexibility, i.e., the possibility of using different materials and fabrication processes. Thanks to its geometrical features, the device offers a satisfactory convective mixing also at relatively low Reynolds numbers. Numerical simulations were performed (1) to get insights into vortices' phenomena and fluid mixing mechanisms and (2) to test the mixing efficiency over a wide range of working conditions. Besides the mixing efficiency, we propose the evaluation of the lacunarity (Allain and Cloitre 1991) to quantify particles dispersion within the micromixer. Using a simple and reliable fabrication process prototypes of the micromixer were also fabricated and the mixing efficiency was experimentally evaluated by applying the microscopic- Laser-Induced-Fluorescence (μ LIF) technique.

2 Material and methods

2.1 Micromixer design

It is well known that in a curved channel the flow undergoes a centrifugal displacement of the maximal axial velocity (Dean 1928). This perturbation leads to the onset of secondary flows because of the unbalance of the centrifugal force and radial gradient of the static pressure. The idea behind the micromixer design proposed here is based on the use of a planar unit cell characterized by two curved, clothoid-shaped segments that allow to exploit convective phenomena such as secondary flows to fold and stretch fluid streams, thus increasing the area interested by diffusion and reducing the thickness of the diffusion boundary layer. Technically, along a clothoid-shaped segment, the curvature k increases linearly with the curvilinear coordinate. This feature allows, even at constant Reynolds values, for the Dean number to increase together with the curvature determining an increase of the secondary flow, being the dimensionless Dean number Dn proportional to the square root of curvature k as it follows:

$$Dn = \frac{UD}{\nu} \sqrt{\frac{D}{R}} = Re\sqrt{kD} \quad (1)$$

where Re is the Reynolds number, D the hydraulic diameter, $R=k^{-1}$ the radius of curvature, U the average velocity, ν the fluid kinematic viscosity. Using curved, clothoid-shaped microchannels as basic segments for secondary flow generators in micromixers has several conceptual advantages. In particular it can be demonstrated that they (1) promote efficient mixing with footprint in the downstream direction shorter than fixed-curvature microchannels and (2) are less prone to kinematic reversibility effects, which affect mixing efficiency. The proof for conceptual advantages mentioned at points 1 and 2 is given in the Appendix. Figure 1(a) shows the schematics of the micromixer design, highlighting its basic characteristics: three inlet segments, four identical mixing units and one outflow segment. Each mixing unit (1 mm length) is composed by two clothoid and two straight segments. The total length of the micromixer is equal to 7.35 mm. The side inlet segment has a width of 100 μ m, while main, outlet and mixing unit channels have all a width of 200 μ m; the channels height is set equal to 145 μ m. The main advantages of using a micromixer design as in Fig. 1 is in the high modularity of the unit cells that (1) use clothoid shaped segments as secondary flow generators and (2) exploit the principle of the split and recombine between two consecutive units to enhance mixing.

2.2 Numerical setup

The finite volume method was adopted to solve the governing equations of the phenomenon, i.e., the coupled Navier–Stokes and mass convection–diffusion equations:

$$\nabla \cdot \mathbf{v} = 0 \quad (2)$$

$$\rho(\mathbf{v} \cdot \nabla)\mathbf{v} = -\nabla p + \mu \nabla^2 \mathbf{v} \quad (3)$$

$$(\mathbf{v} \cdot \nabla)c = D \nabla^2 c \quad (4)$$

where \mathbf{v} and p are the velocity vector and the pressure in each point of the fluid domain, respectively; ρ and μ are fluid density and viscosity, respectively; D is the diffusion coefficient and c denotes concentration. The general purpose CFD code Fluent (ANSYS Inc., USA) was used. The three-dimensional geometric model of the micromixer and the computational grid (hexahedral cells, mesh cardinality equal to 2,700,000) were generated using the solid modeler GAMBIT (ANSYS Inc., USA). Simulations were performed at steady-state, laminar conditions, neglecting body force contributions. Mixing was evaluated by modelling the presence of two (isotropic, incompressible, newtonian) fluidic species both with a density value equal to 998 kg m⁻³ and a dynamic viscosity value equal to 10⁻³ kgm⁻¹s⁻¹. Diffusivity of the mixture was set equal to 4×10⁻¹⁰ m²s⁻¹. The SIMPLEC scheme was applied for pressure–velocity coupling. Second-order discretization method for pressure and second-order upwind for velocity and concentration was applied. Twelve different flow regimes (Reynolds number ranging from 1 to 110) were simulated by applying Dirichlet conditions at inlet sections (as flat velocity profiles) while the reference pressure Neumann boundary condition was imposed at the outlet section. Walls were assumed to be rigid, and the no-slip condition was imposed. To quantify mixing potency, one species A was inserted in the main inlet, whereas the second one B was introduced in the side inlets. The species concentration in the simulations was expressed in terms of mass fraction, so that for instance the concentration of the species A (B) would be 1 (0) at the main inlet and 0 (1) at the side inlets. Mixing was considered uniform whenever the concentration of AOB0.5. In particular, in each micromixer cross-section (i.e., normal to the direction of the flow), the mixing efficiency ME was given by (Chung and Shih 2007):

$$ME = 1 - \sqrt{\frac{1}{N} \sum_{i=1}^N \left(\frac{c_i - \bar{c}}{\bar{c}} \right)^2} \quad (5)$$

where N is the number of sampling points, c_i is the mass fraction of species at the point i th belonging to one cross-section of the device, and \bar{c} is the average mass fraction of species. The ME was evaluated at three cross-sections along the micromixer. Lacunarity index (LAC) measures how much the distribution of particles into a fluid stream is uniform, clustered or dispersed. In practice, to calculate LAC the main inlet section of the micromixer was seeded with a set of 800 inert particles and grids with same number of cells and dimensions were created over several micromixer crosssections, where calculations of LAC were performed. Afterwards a binary map was created where each grid cell was denoted with zero or one, depending on the absence or the presence of particle content respectively. Over each binary map the ‘gliding box’ protocol (Allain and Cloitre 1991) was applied as follows: (1) a box equal to the area of four mesh cells was superimposed to the map; (2) starting from the upper left-hand corner, the box was moved one unit to the right (with a unit corresponding to the grid cell size) and the number of grid cells containing zeros and ones was counted (Plotnick et al. 1993); (3) the box was shifted down one grid cell size when the end of a row was reached and the process was repeated until the box covered the entire map; (4) a frequency distribution of the number of the zeros or ones grid cells within the box was obtained and converted to a probability distribution. LAC was finally calculated as:

$$LAC = 1 + \frac{\sum_n n^2 P(n, r)}{(\sum_n n P(n, r))^2} \quad (6)$$

where n is the number of grid cells in a gliding box of size r (in this application $r=r$ corresponds to the area of four grid cells, i.e. $r=2$), and $P(n, r)$ is the probability function of the grid cell distribution. From Eq. 6, the second term of the LAC represents the ratio between the second moment and the square of the first moment of the distribution P . LAC value, that can be equal or greater than one, has the physical meaning of the scatter of seeded (and transported) particles

onto microchannel crosssections. Technically, the greater the degree of particle dispersion, the lower the value of LAC: a value of LAC equal to 1 indicates a uniform dispersion of particles over the crosssection of the channel (the second moment, i.e., the variance of the distribution, is null), while a value of LAC greater than 1 indicates non-uniformity in the distribution of particles.

2.3 Fabrication process

Figure 1(b) shows a fabricated micromixer prototype. The prototypes for the experimental investigation were fabricated using single-step soft lithography. A two-dimensional microchannel pattern was generated using a CAD software (AutoCAD, Autodesk Inc) and printed onto a transparency mask (resolution equal to 32,512 dpi). A master for replica molding was prepared from negative photoresist (SU-8, Microchem) spun up to a thickness of 145 μm on a 4-inch silicon wafer, by transferring the mask pattern through standard photolithography. Microfluidic devices were then fabricated from PDMS (Sylgard 184, two-part elastomer) by replica molding (Xia and Whitesides 1998; Whitesides et al. 2001). The master mold was initially placed in a saturated atmosphere of trichlorotrimethylsilane (Sigma-Aldrich) for 10 min to minimize adhesion of the PDMS to the SU-8 pattern. A 10:1 PDMS monomer/catalyst mixture was prepared, degassed, and poured on the master mold up to an approximate thickness of 5 mm. The mold was again degassed under vacuum to remove air bubbles, and subsequently baked at 80 $^{\circ}\text{C}$ for 3 h. Once the PDMS was cured, the patterned structure was cut and removed and inlet and outlet ports for fluidic connections were punched with a 25 G Luer stub. After an air plasma treatment (Expanded Plasma Cleaner, Harrick Plasma), the PDMS structure was brought into adhesion against an histology glass slide and baked at 80 $^{\circ}\text{C}$ for additional 30 minutes so to form a covalent bonding between the two layers.

2.4 Experimental setup

In order to experimentally characterize the mixing efficiency of the device, the μLIF technique was used (Sinton 2004). This method provides a visualization of the concentration field of a fluorescent molecular dye, used as a passive scalar transported in the flow. Contrarily to macroscopic LIF, where the measurement plane is defined by a thin laser sheet, μLIF uses volume illumination and the recorded fluorescence intensity is averaged along the optical path in the liquid (Matsumoto et al. 2005). The results were used to verify experimentally the mixing potency of the clothoid design, following the approach used earlier by Jiang et al. (2004). Here, an Observer Z.1 inverted epi-fluorescent microscope (Carl Zeiss AG) equipped with an LD-Plan Neofluar objective (5 \times magnification, numerical aperture equal to 0.16) was used and Rhodamine-B as a fluorescent marker. Technically, a 0.26 $\mu\text{mol l}^{-1}$ concentrated solution of Rhodamine-B in distilled water was introduced in the main inlet, whereas pure distilled water was introduced in the side inlets. The flow was driven by means of a high-precision, pulsation-free, syringe pump (neMESYS, Cetoni GmbH). The illumination was provided by a two cavity frequencydoubled Litron Nano S Nd:YAG laser at a wavelength of 532 nm. The measurements were performed at four Reynolds numbers ($Re=10, 60, 80, 110$). Digital images were captured using a 12-bit, 1376 \times 1040 pixels, interline transfer CCD camera (Sensicam QE, PCO GmbH). An empirical calibration procedure was used to convert the image intensities to concentration values. Assuming the dye concentration constant through the height of the microchannel, the recorded intensity (I) is given by (Matsumoto et al. 2005):

$$I = C_0 + C_1(1 - \exp(-C_2c)) \quad (7)$$

where c is the dye concentration, and C_0, C_1, C_2 are empirical constants depending on the experimental conditions, such as the thickness of the microchannel, the illumination intensity, the background image due to fluorescent emission from the structure material. A calibration curve, reported in Fig. 2, was obtained measuring the fluorescent intensity in the micromixer filled with a solution of water and Rhodamine B at six known concentration values. The values of the empirical constants were obtained by fitting Eq. 7 to the experimental data in Fig. 2.

3 Results and discussion

As a first step, we preliminarily focused on the role played by the clothoid-shaped segment in the first unit cell of the device. The numerical results obtained at $Re=10$ and $Re=100$ for the concentration distribution at four different cross-sections within the first mixing unit are shown in Fig. 3, together with the streamlines visualization. It can be observed that at $Re=10$ the mixing is poor, as confirmed by the only slightly distorted interface between the two fluidic species and by the streamlines, mostly aligned with the axis of the microchannel (Fig. 3 (a)). On the contrary, at $Re=100$ the concentration distribution at the same cross-sections exhibits interfaces between the two fluidic species that are sensibly distorted, highlighting the presence of mixing (Fig. 3(b)). The physical reason for this is the fact that the local increase in the Dean number (depending on the Reynolds number and on the increasing local curvature within the clothoid segment) leads to the onset of counter-rotating Dean vortices: the centrifugal force pushes the outer fluid streams toward the clothoid center and, in turn, the inner fluid streams toward the upper and lower walls of the microchannel. This continuous bending phenomenon, which is source of mixing, can be better observed through the streamlines visualization: streamlines located near the inner wall at the beginning of the mixing unit move toward the outer wall. The advantage offered, in terms of mixing enhancement, by the split and recombination phenomenon within the device is shown in Fig. 4. Streamlines clearly display that recirculation regions between the first two mixing units are

present both at $Re=10$ (Fig. 4(a)) and $Re=100$ (Fig. 4(b)). In particular the latter case is characterized by an highly three-dimensional flow field, with an enhanced stretching and folding of the vortex structures when the fluid moves from one unit to the adjacent one. The mixing enhancement along the microdevice is displayed in Fig. 5 in terms of concentration colour maps at three different cross-sections. It can be observed that fluids interface at the beginning of the first mixing unit are distorted at different levels, depending on the value of the Reynolds number. At $Re=10$ the interface distortion is still moderate even at the exit of the fourth mixing unit (Fig. 5(a)). On the contrary at $Re=100$ the combined effect of secondary flows and recirculation regions, which are stretched and folded (due to (1) the varying-with-length curvature of the clothoid segments and (2) to the split and recombination of fluid streams) on the concentration distributions is clearly evident: at the outlet section of the last mixing unit the concentration distribution is rather homogeneous (Fig. 5(b)). Qualitative information about the mixing efficiency of the device in relation to its working conditions can be obtained by visual inspection. Figure 6 shows the maps of the concentration distribution at the outlet section of the micromixer (section E) as obtained *in silico* at Reynolds numbers in the range 1–100. It can be observed that in the simulated transport the two species become less segregated as Re increases. Figure 6 shows that at flow regimes characterized by Reynolds numbers greater than 50 the two fluidic species are well mixed (homogeneous concentration distribution), and it becomes hard to distinguish their interface. The qualitative analysis based on Fig. 6 is confirmed by calculations of mixing efficiency. Figure 7 shows the values of ME in the micromixer, in correspondence of three crosssections (i1, i3, E), at different Reynolds numbers. It can be noticed that in general mixing increases both with the distance from the inlet and with the Reynolds number. In particular, ME grows significantly from the inlet section (i1) to the outlet one (E). Interestingly, ME is lower at $Re=5$ than at $Re=1$ both at sections i3 and E. Indeed, this phenomenon is not new: whereas at $Re \approx 1$ mixing is dominated by molecular diffusion and at Reynolds greater than 10 there is a strong influence of convective phenomena, at $Re \approx 5$ there exists a sort of equilibrium between convective and diffusive phenomena (Chung et al. 2008). Through the evaluation of ME values it is possible to exploit the role played by individual mixing units as a function of the Reynolds number. At the inlet of the first unit (i1), ME is almost independent of the Reynolds number, confirming in part recent studies (Bothe et al. 2006; Hoffmann et al. 2006). In fact, the value of ME at section i1 is low even for $Re=100$ because there is no formation of those secondary flows that normally occur, for example, in T-mixers (in the form of double vortex pairs) above a critical Reynolds number, due to instabilities caused by centrifugal forces (Bothe et al. 2006; Hoffmann et al. 2006): indeed, the inlet of the micromixer proposed here differs from a traditional T-mixer in the presence of three inlets, with the central flow regulating the action of the competitive flows from the side channels. The dispersion of particles at the outlet section (E), as obtained at different Reynolds number does give further information of the mixing potency of the device. At $Re=10$ particles tend to gather mainly in the centre of the outlet section and in proximity of the upper and lower walls (Fig. 8(a)). On the contrary, at $Re=100$ particles occupy the entire outlet section, i.e. they are completely dispersed (Fig. 8(b)). The qualitative analysis on the distribution of the particles is confirmed by the quantitative calculation of the lacunarity. This is because if we consider that particles transported into a fluid stream can be uniformly clustered or dispersed, LAC can provide a measure of their spatial distribution as a surrogate measure of mixing. LAC was originally developed to quantify the geometric arrangement of gaps (lacunae) in solid objects (Mandelbrot 1983). This index was then adopted to describe gaps in habitat coverage, providing a way to quantify landscape texture and to evaluate habitat dispersion at multiple scales in the terrestrial ecosystems (Plotnick et al. 1993). Figure 9 shows the values of LAC obtained in correspondence of six cross-sections along the micromixer at two different flow regimes ($Re=10$ and $Re=100$). It is worth noting that LAC shows a decreasing trend along the micromixer for both the two flow regimes. However, while at $Re=10$ the LAC value is around 2 at the outlet section (E) of the micromixer, at $Re=100$ LAC is equal to 1.1, i.e. very close to the threshold value $LAC=1$ corresponding to a uniform dispersion of particles (see Eq. 6). This is an interesting result that confirms the conclusions also obtained by calculation of the mixing efficiency and candidates lacunarity as quantitative descriptor of mixing in microdevices. An experimental characterization of the mixing phenomena into the device was performed by applying the μ LIF technique. Micrographs of the device at $Re=10$, 80 and 110 operating conditions are shown in Fig. 10. It can be noticed that at $Re=10$, the convective mixing is negligible and the dye at the outlet is mainly concentrated in the central part of the channel (Fig. 10, upper panel). At $Re=80$ the presence of convective mixing can be clearly observed looking at the complex flow-patterns forming already after the section i1 (Fig. 10, mid panel). In this case, the dye at the outlet is more distributed along the whole width of the channel, although a higher concentration is still noticeable in the axis region. A complete mixing at the outlet can be observed at $Re=110$ (Fig. 10, lower panel). A quantitative evaluation of the dye concentration in different cross-sections of the device was also performed. The concentration profiles at section i1 and at the outlet section E, measured at four different flow conditions, are shown in Fig. 11(a) and (b). While the concentration profiles show a weak dependence on the Reynolds number at the inlet section i1 (Fig. 11(a)), with a constant dye concentration of approximately $0.26 \mu\text{mol l}^{-1}$ in the central part of the channel (estimated random error of $\pm 0.03 \mu\text{mol l}^{-1}$), at the outlet section concentration is strongly dependent on the Reynolds number. In fact, at section E, the dye is still concentrated in the central part of the inlet at $Re=10$, while at $Re=60$ and 80 the dye is more distributed along the whole section of the microchannel, with a minimum concentration of $0.07\text{--}0.08 \mu\text{mol l}^{-1}$. A concentration peak is however still present in the centre of the channel (Fig. 11(b)). At $Re=110$ the dye is evenly distributed, with an average concentration of $0.13 \mu\text{mol l}^{-1}$, and an estimated ME of 0.76 (Fig. 11(b)). The experimental results indicate that for the micromixer prototype a mixing efficiency of 80 % is obtained at $Re=110$, in good agreement with the numerical results.

Figure 11(c) and (d) shows a direct comparison between experimental and numerical concentration profiles at $Re=10$ and 110. In order to match the experimental results, which are depth-averaged, the numerical concentration profiles were obtained calculating the mean concentration along the channel height. Discrepancies in the concentration profiles are clearly expected, due to the uncertainty of the measurement method and to small deviations of the experimental operating and boundary conditions (such as fluctuation in the actual flow rate due to the syringe pump or inaccuracy in the channel geometries due to manufacturing process). However, the overall trend of the experimental profiles is well caught by the numerical simulation as can be observed in Fig. 11 (c) and (d). Hence the experimental investigation, showing a good agreement with the numerical results, confirms that the design principles of the proposed micromixer are suitable to induce effective passive convective mixing at low Reynolds numbers, as a consequence of onset and development of secondary flow patterns and recirculation. For the sake of completeness, here we report a comparison of recently proposed passive planar micromixer designs with the one proposed here. The geometric features of three recently proposed microdevices (Chung et al. 2008; Ansari et al. 2010; Fan and Hassan 2010) are summarized in Table 1. The mixing efficiency at different flow regimes of passive planar micromixer designs summarized in Table 1 is shown in Fig. 12. It can be observed that the micromixer proposed here is characterized by a mixing efficiency that is comparable, when not superior, to the other micromixer designs and that this comparable/superior performance is obtained with geometric features, i.e., footprint and total length, that are less microchip space consuming with respect to the other devices (Table 1). In fact, the device proposed by Ansari et al. (2010), based on the unbalanced collision principle generated by circular sub-channels with different widths, is characterized by a 65%ME when six circular mixing units are used. Also Chung et al. (2008) achieved a good mixing efficiency in a three-rhombi micromixer with a converging–diverging element only at Reynolds numbers of about 200, while optimizing the design with Taguchi method, i.e., increasing the number of rhombic unit cells with a 60° turning angle (and the microdevice length as a consequence, up to 13.5 mm), a 90 % of ME was reached at Reynolds numbers in the order of 80 (Chung et al. 2008). The micromixer design proposed here combines some important factors including device footprint (i.e. reduction of mixing unit and length as consequence) and the possibility of using different materials and fabrication method (i.e. planar microchannels). In fact, most micromixer has been often achieved through the implementation of geometrical features to microchannels aiming at perturbing the laminar flow (Liu et al. 2000; Stroock et al. 2002). Devices provided with such features demonstrated high mixing potency at specific flow conditions (low and medium Reynolds regimes). However, the fabrication process required for their fabrication is often limited to soft-lithography techniques, and the subsequent choice of the materials to be processed is limited. The single layer microfluidic device category can be easily achieved through several microfabrication techniques, including lithographic processes (Whitesides et al. 2001), laser ablation (Selimović et al. 2011), wet and dry etching (Lin et al. 2001), mechanical micromilling (Wilson et al. 2011), cutting-plotting (Piraino et al. 2012). As a consequence, the wide choice of suitable techniques allows the user to select the appropriate material for the specific application, ranging from silica-based substrates to hard and soft plastic materials.

4 Conclusion

A new passive microfluidic mixer design with a modular architecture based on microfluidic units of curvature- varying-with-length (clothoids) segments was analysed both computationally and experimentally. The mixing efficiency of the prototype was experimentally evaluated by applying the microscopic-Laser-Induced-Fluorescence (μ LIF) technique. The micromixer exploits its geometric features to ensure proper mixing efficiency by promoting the “bending phenomenon” at the interface between species (thus assuring an increased interface length suitable for mixing) caused by secondary flow in the unit cell and recirculation effects in the junction of the unit cell. Here we demonstrated that the proposed design assures a mixing efficiency that is comparable, if not superior, to other passive planar micromixer designs and that this performance is obtained with small microdevice footprint. In addition, the herein proposed LAC index corroborated mixing efficiency results and has proven its suitability not only as quantitative descriptor of particles dispersion in the streaming fluid, but also as powerful tool to evaluate overall mixing. The device belongs to the single layer microfluidic device category, where a bidimensional layout is extruded in the third dimension, and can be fabricated using several microfabrication techniques, thus allowing the user to select the appropriate material for the specific application.

Appendix

An advantage in using clothoid microchannels as basic segments in micromixers is related to the possibility for secondary flows generation (and mixing promotion as a consequence) with footprint in the downstream direction shorter than fixed-curvature (ring) microchannels. A curved microchannel is characterized by two parameters, i.e., curvature and length. To compare the performance, in terms of mixing efficiency, of a fixed-curvature microchannel (Fig. 13, geometry A) as studied by Schönfeld and Hardt (2004) and a clothoid microchannel with the same hydraulic diameter, the influence of geometric features was analyzed disjointedly. In detail, clothoid microchannels with (1) the same length (Fig. 13, geometry B) as and (2) initial curvature as fixed-curvature microchannel (Fig. 13, geometry C) were investigated. Table 2 shows the values of the parameters taken in consideration in this example. Figure 13 clearly shows that an advantage of clothoid microchannels is that they have a footprint lower than fixed-curvature microchannels, in the downstream direction (length footprint (L_{fp}) is almost 20%(clothoid B) and 40%(clothoid C) lower than ring microchannel (A); the length of clothoid channel C is almost the 60%of ring channel A length).A L_{fp} of

clothoid microchannels lower than fixed-curvature geometries could represent a real advantage in fabrication process when micromixers based on convective mixing have to be incorporated into a microchip. This is an important aspect because, in general, mixing efficiency is evaluated in terms of minimum mixing distance. To demonstrate the potency of clothoid microchannels as basic units for mixing generation, we (1) performed CFD simulations and (2) used computational results to estimate the effect of secondary flows on convective mixing in the three microchannel geometries summarized in Table 2. CFD simulations were performed by solving the same equations as described in the Materials and Methods section, mimicking the presence of two different fluids. As an example of the results obtained from simulations, Fig. 14 shows the concentration distribution of the two fluids and the interface deformation at the outlet section, at the same flow regime ($Re=75$). It can be noticed that the shape of the interface is very similar at the outlet section of fixed-curvature (A) and clothoid microchannels (B, C). In clothoid microchannels, the fluid experiences an increase in the channel curvature as it flows downstream, accompanied by an increased amount of secondary flows. To quantify the convective effect of secondary flows on mixing, we defined a dimensionless quantity, the Interfacial gain (I_G), a measure of the increment of interface area for unitary length of the channel. Being $L(s)$ the length of the curve given by the intersection between the miscible streams and the channel cross section at the generic channel length s (i.e., the interface length), I_G can be expressed as

$$I_G = \frac{1}{D} \left(\frac{dA}{ds} - D \right) = \frac{L(s)}{D} (r_c(s) \chi(s) + 1) - 1 \quad (8)$$

where D is the characteristic length of the microchannel cross section, A is the interface area, r_c is the radial coordinate of the centroid of the interface line $L(s)$. The interface area depends upon the radius of curvature of the interface line centroid via the Pappus's centroid theorem. The length of the interface at the inlet section $L(0)$ is equal to D . Roughly speaking, I_G estimates mixing potency from the increment for unit length of interface area. Table 3 summarizes I_G and pressure drop values characterizing the three microchannel geometries in Fig. 13, at the same flow regime ($Re=75$). Notably, the clothoid microchannels exhibit performances that are comparable to the fixed-curvature microchannel both in terms of mixing potency and in terms of pressure drop, but with a lower footprint. Another reason leading us to use clothoid segments into the micromixer design proposed here is that we observed that in clothoid-shaped meander micromixers the mixing reversal effect observed in devices using fixed-curvature segments (Yamaguchi et al. 2003; Yamaguchi et al. 2004) is attenuated and, as a consequence, the mixing efficiency increased. In detail, we started from findings by Yamaguchi and coworkers (Yamaguchi et al. 2003; Yamaguchi et al. 2004) that at low and intermediate Reynolds flow regimes the interface between two fluids streams in double-curved microchannels with fixed-curvature segments undergo a reversal of the convective phenomenon and, as a consequence, of a convective mixing reversal effect (Fig. 15). In detail, it was observed both experimentally and in silico that the initial interface between two fluids at the inlet section of a meander microchannel made of two fixed-curvature segments was stretched and folded at the outlet of the first curved segment while the effect of the second curved segment was of stretching and folding the interface nullifying the convective effect of the first segment, because inertial forces were exerted in opposite directions; (2) on the contrary, at relatively high Reynolds number, the interface was wave-shaped and kinematic reversibility was marginal in the mixing of fluids. Here, the kinematic reversibility in a meander micromixer unit made of two clothoid segments with geometric features as model B in Table 2 was compared with the reversibility occurring in the meander micromixer proposed by the group of Yamaguchi (Yamaguchi et al. 2003; Yamaguchi et al. 2004) and made of segments with geometric features as model A in Table 2. To do it, we used the same approach as for the study on single clothoid and fixed-curvature microchannels. Figure 16 shows the distribution of the fluid streams at the outlet section of the two meander microchannels: at relatively low Reynolds flow regimes ($Re < 10$) the kinematic reversibility is almost complete, independent of the geometric features of the segments. Anyway, by increasing the flow rate ($Re > 25$), kinematic reversibility is more attenuated in the clothoid-shaped meander microchannel than in fixed-curvature-shaped. It was found that (1) at intermediate Reynolds flow regimes ($Re = 10$) the increment of interface area for unitary length (I_G) increases to almost 1 during the first segment while in the segment with curvature reversal the I_G decreases to almost zero, independent of the geometry of the segment; (2) at relatively high Reynolds flow regimes ($Re = 75$), at the outlet section of the clothoid-shaped meander microchannel the I_G is about 20 % higher than fixed-curvature-shaped meander microchannel (2.18 against 1.82). A further analysis was carried out in order to get insight into the physical reason at the basis of the observed reduced reversibility in clothoid-shaped meander microchannels. To do it, we calculated the mean value of the streamwise vorticity (STWV) at several cross sections along the curvilinear coordinate s of both the clothoid and fixed-curvature segments B and A (Fig. 13), respectively. As mentioned above, here we took advantage of the existence of a symmetry plane so that STWV was calculated on half of each cross section of microchannels as:

$$STWV = \frac{1}{S} \int_S \frac{|\mathbf{v} \cdot (\nabla \times \mathbf{v})|}{|\mathbf{v}|} dS \quad (9)$$

where S is the area of half of the microchannel cross section. Our findings show that the $STWV$ increases almost linearly with the curvilinear coordinate s in the clothoid segment, while in the fixed-curvature segment the $STWV$ reaches a plateau at about two diameters downstream of the inlet section and remains at almost the same value up to the outlet section, where the $STWV$ in the clothoid is considerably higher than the fixed-curvature segment (Fig. 17). It is this increased generation of local streamwise vorticity into the clothoid microchannel the responsible for the reduced kinematic reversibility observed in the clothoid-shaped meander micromixer in Fig. 15.

References

- C. Allain, M. Cloitre, *Phys Rev A* 44, 3552 (1991)
- M.A. Ansari, K.-Y. Kim, K. Anwar, S.M. Kim, *J Micromech Microeng* 20, 055007 (2010)
- F.G. Bessoth, A.J. de Mello, A. Manz, *Anal Commun* 36, 213 (1999)
- D. Bothe, C. Stemich, H.-J. Warnecke, *Chem Eng Sci* 61, 2950 (2006)
- C.K. Chung, T.R. Shih, *J Micromech Microeng* 17, 2495 (2007)
- C.K. Chung, T.R. Shih, *Microfluid Nanofluid* 4, 419 (2008)
- C.K. Chung, T.R. Shih, T.C. Chen, B.H. Wu, *Biomed Microdevices* 10, 739 (2008)
- C.K. Chung, T.R. Shih, B.H. Wu, C.K. Chang, *Microsyst Technol* 16, 1595 (2010)
- W.R. Dean, *Philos Mag* 5, 673 (1928)
- Y.F. Fan, I. Hassan, *Exp Fluids* 49, 733 (2010)
- A. Gigras, S. Pushpavanam, *Microfluid Nanofluid* 5, 89 (2008)
- S. Hardt, K.S. Drese, V. Hessel, F. Schönfeld, *Microfluid Nanofluid* 1, 108 (2005)
- V. Hessel, H. Löwe, F. Schönfeld, *Chem Eng Sci* 60, 2479 (2005)
- M. Hoffmann, M. Schlüter, N. Rübiger, *Chem Eng Sci* 61, 2968 (2006)
- P.B.J. Howell, D.R. Mott, J.P. Golden, F.S. Ligler, *Lab Chip* 4, 663 (2004)
- F. Jiang, K. Drese, S. Hardt, M. Küpper, F. Schönfeld, *AIChE J* 50, 2297 (2004)
- D.S. Kim, S.H. Lee, T.H. Kwon, C.H. Ahn, *Lab chip* 5, 739 (2005)
- M.G. Lee, S. Choi, J.-K. Park, *Biomed Microdevices* 12, 1019 (2010)
- C.H. Lin, G.B. Lee, Y.H. Lin, G.L. Chang, *J Micromech Microeng* 11, 726 (2001)
- C.H. Lin, C.H. Tsai, L.M. Fu, *Biomed Microdevices* 9, 43 (2007)
- R.H. Liu, M.A. Stremler, K.V. Sharp, M.G. Olson, J.G. Santiago, R.J. Adrian, H. Aref, D.J. Beebe, *J Microelectromech S* 9, 190 (2000)
- R.H. Liu, J. Yang, M.Z. Pindera, M. Athavale, P. Grodzinski, *Lab Chip* 2, 151 (2002)
- P. Löb, K.S. Drese, V. Hessel, S. Hardt, C. Hofmann, H. Löwe, R. Schenk, F. Schönfeld, B. Werner, *Chem Eng Technol* 27, 340 (2004)
- B.B. Mandelbrot, *The Fractal Geometry of Nature* (W. H. Freeman and Company, San Francisco, 1983)
- S.L. Marasso, E. Giuri, G. Canavese, R. Castagna, M. Quaglio, I. Ferrante, D. Perrone, M. Cocuzza, *Biomed Microdevices* 13, 19 (2011)
- R. Matsumoto, H. Zadeh, P. Ehrhard, *Exp Fluids* 39, 722 (2005)
- X. Niu, Y.-K. Lee, *J Micromech Microeng* 13, 454 (2003)
- N.-T. Nguyen, Z. Wu, *J Micromech Microeng* 15, R1 (2005)
- N.-T. Nguyen, *Micromixers : fundamentals, design and fabrication* (William Andrew Micro & Nano Technologies Series, 2008)
- F. Pennella, F. Mastrangelo, D. Gallo, D. Massai, M.A. Deriu, G. FalvoD'UrsoLabate, C. Bignardi, F. Montevicchi, U. Morbiducci, in *Single and two-Phase Flows on Chemical and Biomedical Engineering*, ed. By Dias R, (Bentham, London, 2011) in press.
- F. Piraino, G. Camci-Unal, M.J. Hancock, M. Rasponi, A. Khademhosseini, *Lab Chip* 12, 659 (2012)
- R. Plotnick, R. Gardner, R. O' Neill, *Landscape Ecol* 8, 201 (1993)
- F. Schönfeld, S. Hardt, *AIChE J* 50, 771 (2004)
- Š. Selimović, F. Piraino, H. Bae, M. Rasponi, A. Redaelli, A. Khademhosseini, *Lab Chip* 11, 2325–2011 (2011)
- D. Sinton, *Microfluid Nanofluid* 1, 2 (2004)
- A.D. Stroock, S.K.W. Dertinger, A. Ajdari, I. Mezic, H.A. Stone, G.M.

Whitesides, Science 295, 647 (2002)
A.P. Sudarsan, V.M. Ugaz, Lab Chip 6, 74 (2006)
G.M. Whitesides, E. Ostuni, S. Takayama, X. Jiang, D.E. Ingber, Annu Rev Biomed Eng 3, 335 (2001)
M.E. Wilson, N. Kota, Y.T. Kim, Y. Wang, D.B. Stolz, P.R. LeDuc, O.B. Ozdoganlar, Lab Chip 11, 1550 (2011)
Y.N. Xia, G.M. Whitesides, Annu Rev Mater Sci 28, 153 (1998)
Y. Yamaguchi, F. Takagi, K. Yamashita, H. Nakamura, H. Maeda, K. Sotowa, K. Kusakabe, Y. Yamasaki, S. Morooka, AIChE J 50, 1530 (2003)
Y. Yamaguchi, F. Takagi, T. Watari, K. Yamashita, H. Nakamura, H. Shimizu, H. Maeda, Chem Eng J 101, 367 (2004)

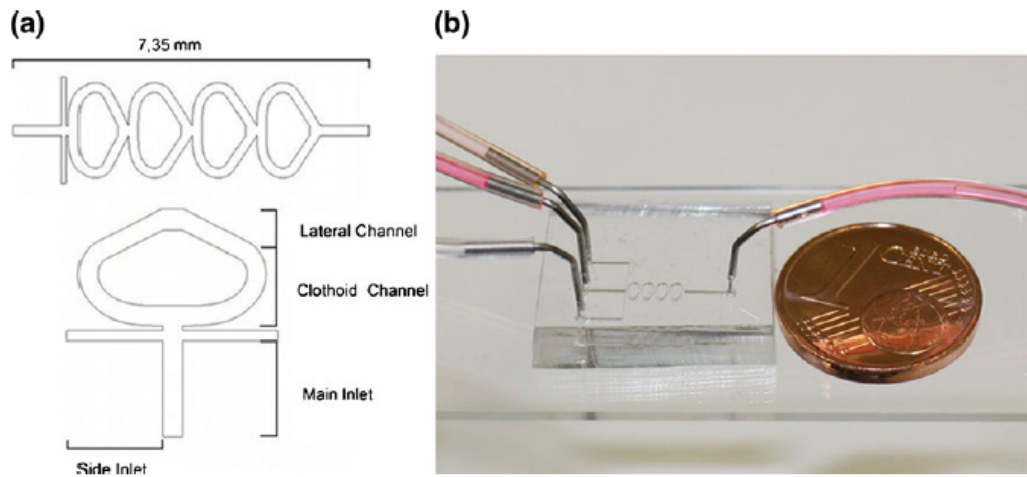


Fig. 1 Channel design (the micromixer top view and particular of the three inlets and clothoid-based cell unit) (a) and micromixer prototype fabricated from PDMS (b)

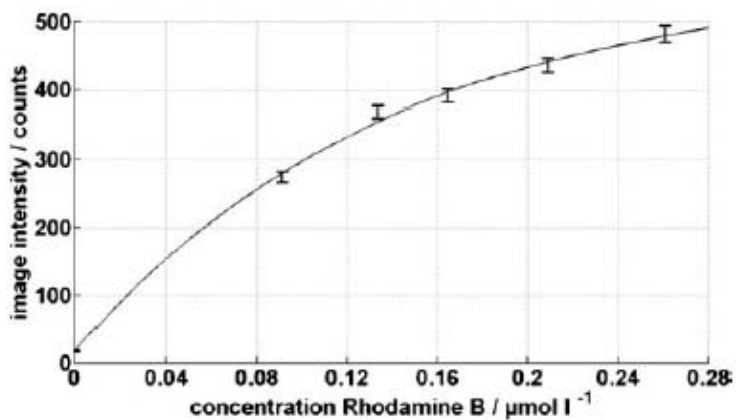


Fig. 2 μLIF calibration: the image intensity depends on the concentration of RhB and the thickness of the measurement volume. The calibration was performed with a homogeneous solution of water and RhB at different concentrations. The thickness of the measurement volume was the height of the channel

Fig. 3 Concentration distributions of three sections along the clothoid channel within the first mixing unit, together with the trajectory distributions color-coded with the local concentration at $Re=10$ (a) (slightly distorted interface and aligned streamlines) and at $Re=100$ (b) (distorted interfaces and twisted streamlines). (For interpretation of the references to color in this figure legend, the reader is referred to the web version of this article)

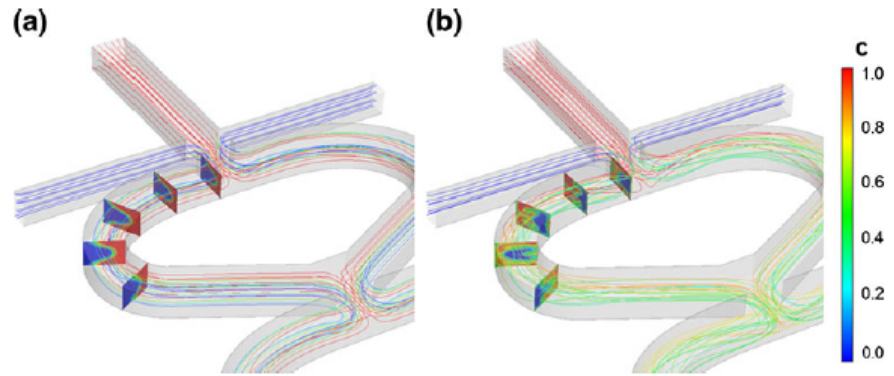
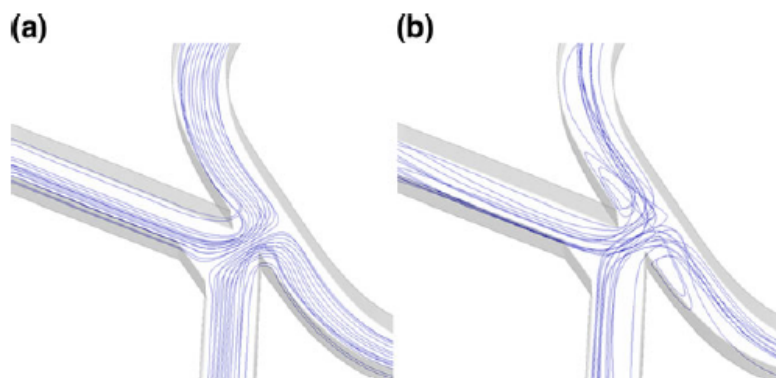


Fig. 4 Top view of the trajectories without vortices trajectories distribution ($Re=10$) and with vortices trajectories distribution ($Re=100$). Trajectories are plotted in correspondence of the end of the second unit



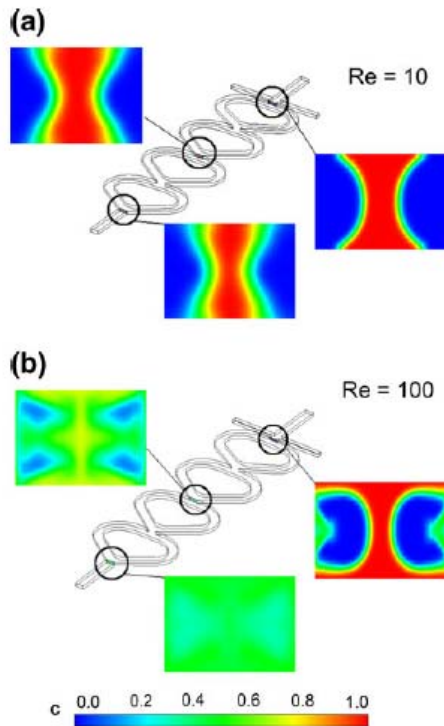


Fig. 5 Comparison among concentration distributions at different recirculation zones at $Re=10$ (a) (moderate distorted interface) and $Re=100$ (b) (fluid mixing is improved by recirculation zones). (For interpretation of the references to color in this figure legend, the reader is referred to the web version of this article)

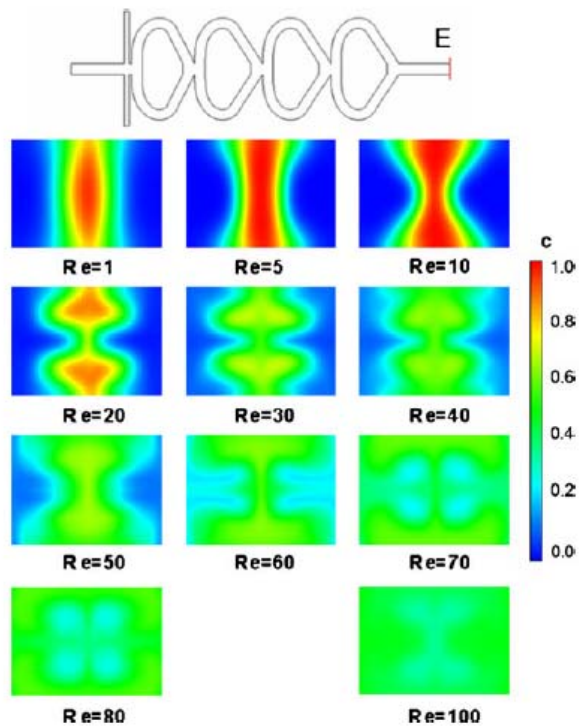


Fig. 6 Comparison of concentration distributions at different Reynolds number of the whole device (section E). The effect of secondary flows in the unit cell and the four recirculation regions is clear at high Reynolds numbers. (For interpretation of the references to color in this figure legend, the reader is referred to the web version of this article)

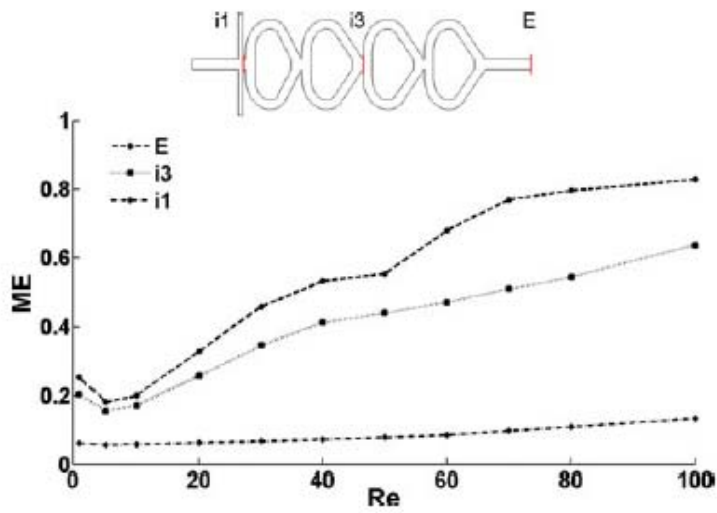


Fig. 7 Mixing efficiency (ME) of the micromixer as a function of Reynolds number in the three cross-sections considered

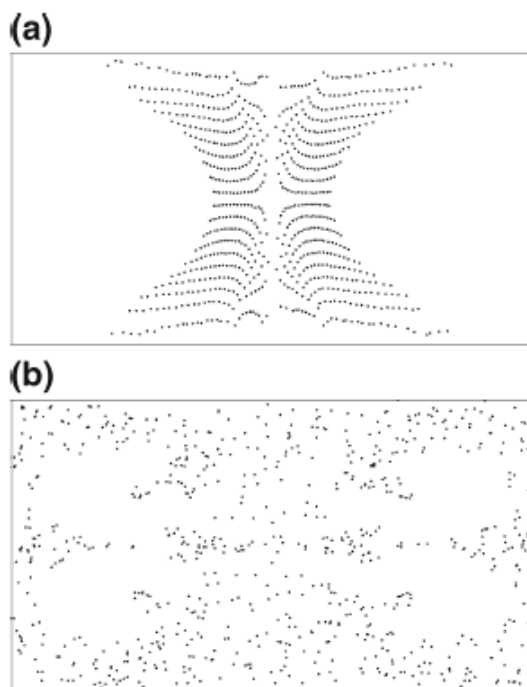


Fig. 8 Micromixer distribution of the particles at section E for $Re=10$ (a) and $Re=100$ (b)

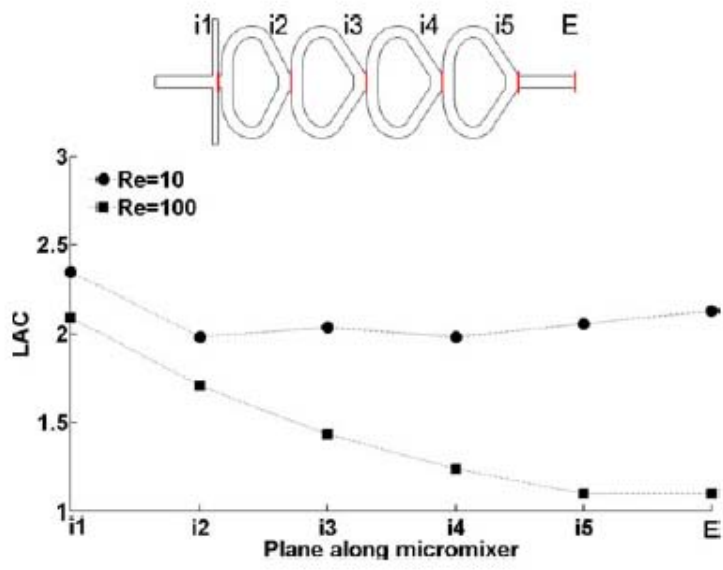


Fig. 9 Lacunarity (LAC) calculated in correspondence of six sections along the micromixer at $Re=10$ and $Re=100$

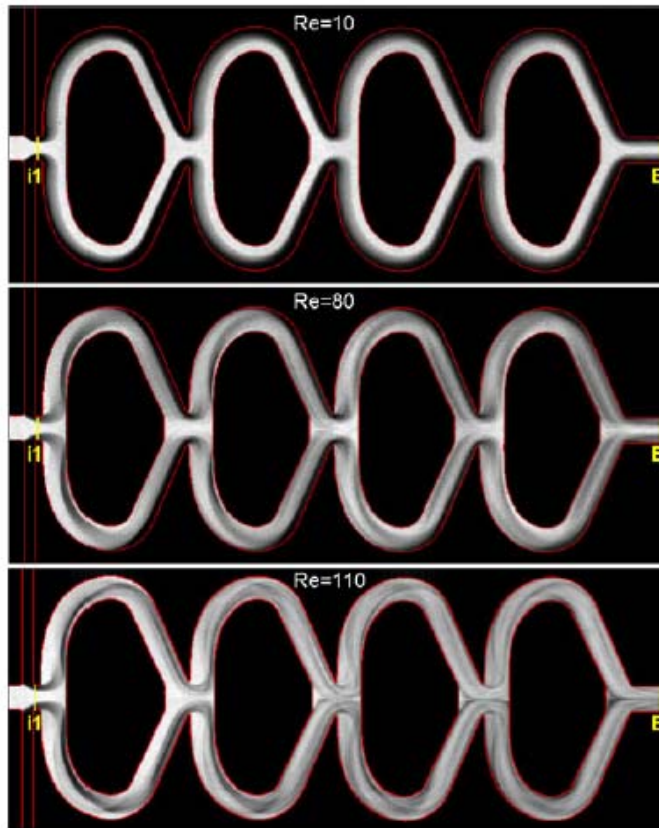


Fig. 10 Micrographs of the micromixer prototype operating at different Reynolds numbers. The contour of the micromixer is shown with a red line. The images are rendered in black and white: the distilled water premixed with RhB at higher concentration (as inserted in the central inlet) corresponds to white, the pure distilled water (as inserted in the lateral inlets) corresponds to black

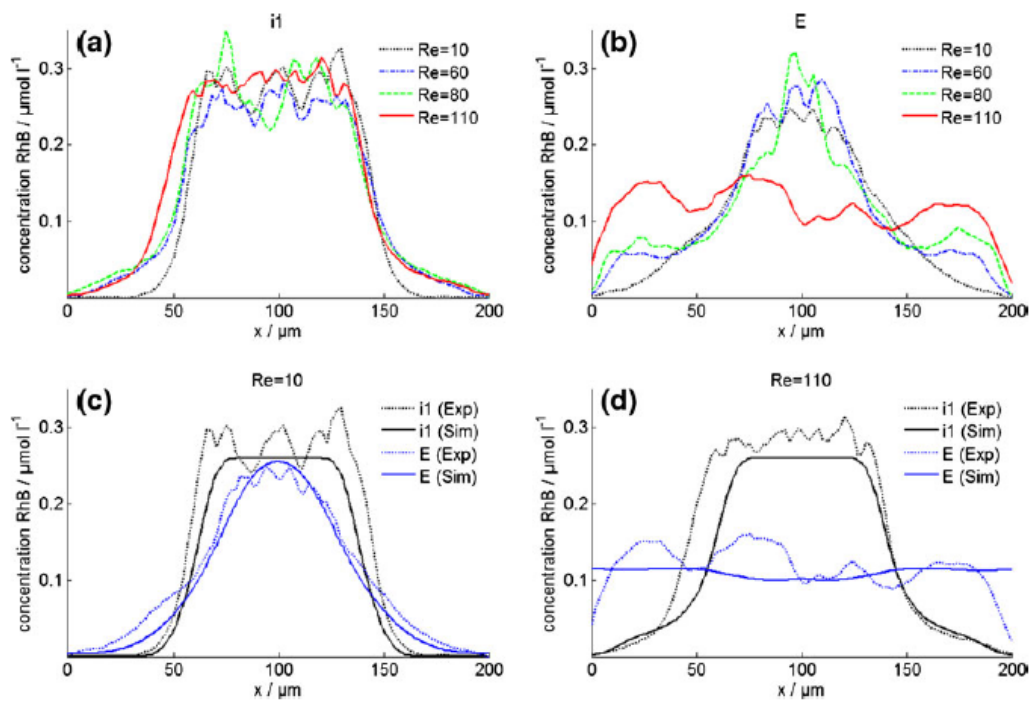


Fig. 11 (a-b) Concentration profiles at the inlets' section (i1) and exit (E) at different Reynolds numbers. At $Re=10$ (E section), the dye concentration is in the central part of the inlet, while at $Re=110$ the dye is well-distributed (average concentration of $0.13 \mu\text{mol l}^{-1}$). (c-d)

Concentration profile comparison between experimental and simulation results at $Re=10$ and $Re=110$. (For interpretation of the references to color in this figure legend, the reader is referred to the web version of this article)

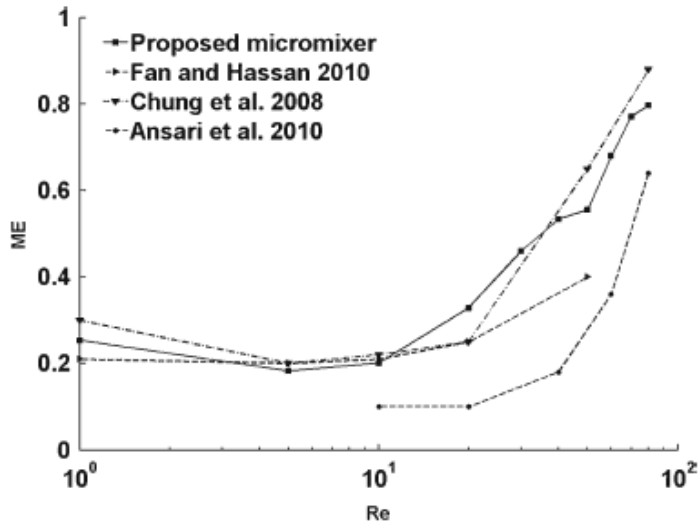


Fig. 12 Mixing efficiency (*ME*) comparison of the micromixer proposed here with micromixer from very recent literature at different Reynolds flow regimes

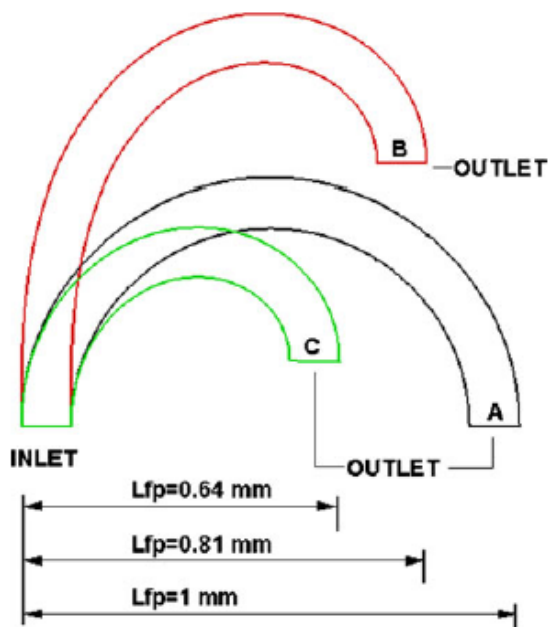


Fig. 13 Footprint in downstream direction: comparison between fixed-curvature segment (a), clothoid with the same length as fixed curvature segment (b) and clothoid with initial curvature as the fixed-curvature segment (c)

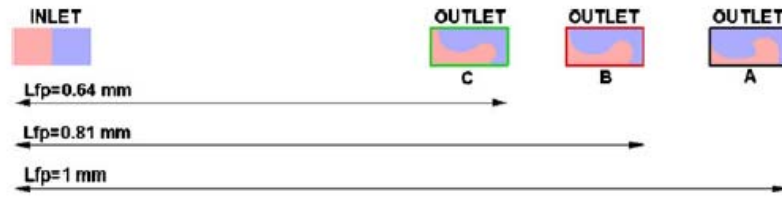


Fig. 14 Interface deformation at the outlet section of (a) the fixed-curvature segment, (b) the clothoid segment with same length as geometry A and (c) the clothoid segment with initial curvature as curvature of

geometry A. (For interpretation of the references to color in this figure legend, the reader is referred to the web version of this article)



Fig. 15 A meander micromixer unit, made of two fixed-curvature segments operating at $Re=10$. Two coloured stream are inserted at the inlet section (left side) and in consequence of secondary flows undergo an increment of contact area which reduces during the reversal of curvature showing kinematic reversibility

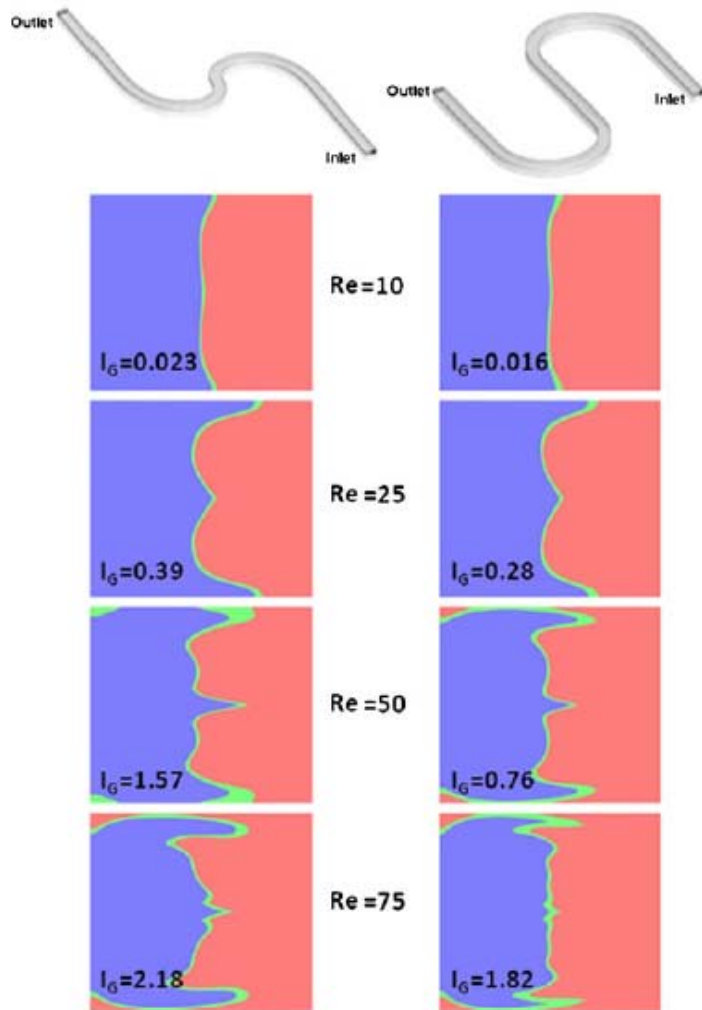


Fig. 16 Spatial distribution of two immiscible species at the outlet section of the two meander microchannels: for fast flows ($Re > 25$) the different curvature modulation induces changes in the final distribution of fluids cancelling out the kinematic reversibility. (For interpretation of the references to color in this figure legend, the reader is referred to the web version of this article)

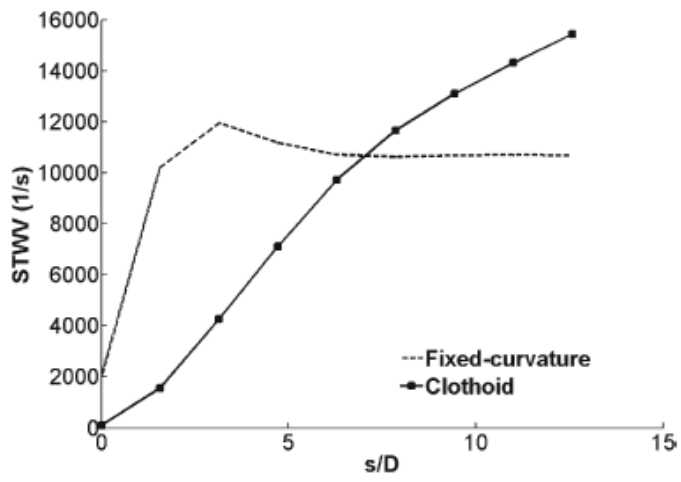


Fig. 17 STWV at several cross sections along fixed-curvature and clothoid microchannel segments ($Re=75$)

Table 1 Summary of recent micromixer designs (Chung et al. 2008; Ansari et al. 2010; Fan and Hassan 2010). The “other elements” column highlights elements in addition to the cell units necessary to improve mixing

Source	Re	Number of unit cell	Footprint unit cell [mm]	Total length [mm]	Other elements
Chung et al. (2008)	0.1–100	4	1.5 · 2.6	13.5	Diverging element
Ansari et al. (2010)	1–80	4 or 6	1.2 · 1.2	8 or 10	Different ratio of widths of sub-channels
Fan and Hassan (2010)	1–50	6	33 · 21	199	Omega structure
Proposed micromixer	1–100	4	1.2 · 1.9	7.3	–

Table 2 Geometric features of the investigated microchannels: length, hydraulic diameter and dimensionless curvature $\chi=D/R$, where D is the hydraulic diameter and R is radius of curvature)

Geometry	Length [mm]	Hydraulic diameter [μm]	Initial curvature	Final curvature
A (ring)	1.41	100	0.22	0.22
B (clothoid)	1.41	100	0	0.44
C (clothoid)	0.88	100	0.22	0.49

Table 3 I_G and pressure drop values at intermediate flow regime ($Re=75$) of (A) the fixed-curvature segment, (B) the clothoid segment with same length as geometry A and (C) the clothoid segment with initial curvature as curvature of geometry A

Geometry	I_G	ΔP [Pa]
A (ring)	2.06	3360
B (clothoid)	1.8	3300
C (clothoid)	1.6	2260